

# PROCEEDINGS OF SPIE

[SPIDigitalLibrary.org/conference-proceedings-of-spie](https://SPIDigitalLibrary.org/conference-proceedings-of-spie)

## Validation of eyelids as acoustic receiver locations for photoacoustic-guided neurosurgery

Graham, Michelle, Creighton, Francis, Lediju Bell, Muyinatu

Michelle T. Graham, Francis X. Creighton, Muyinatu A. Lediju Bell, "Validation of eyelids as acoustic receiver locations for photoacoustic-guided neurosurgery," Proc. SPIE 11642, Photons Plus Ultrasound: Imaging and Sensing 2021, 1164228 (5 March 2021); doi: 10.1117/12.2582562

**SPIE.**

Event: SPIE BiOS, 2021, Online Only

# Validation of eyelids as acoustic receiver locations for photoacoustic-guided neurosurgery

Michelle T. Graham<sup>1</sup>, Francis X. Creighton<sup>2</sup>, and Muyinatu A. Lediju Bell<sup>1,3,4</sup>

<sup>1</sup>Department of Electrical and Computer Engineering, Johns Hopkins University, Baltimore, MD, USA

<sup>2</sup>Department of Otolaryngology - Head and Neck Surgery, Johns Hopkins Medicine, Baltimore, MD, USA

<sup>3</sup>Department of Biomedical Engineering, Johns Hopkins University, Baltimore, MD, USA

<sup>4</sup>Department of Computer Science, Johns Hopkins University, Baltimore, MD, USA

## ABSTRACT

Accidental injury to underlying blood vessels and nerves during minimally invasive neurosurgery can have severe surgical complications (e.g., blindness, paralysis, and death). Transcranial photoacoustic imaging is a promising technique for real-time visualization of these structures, but it is challenged by acoustic-bone interactions which degrade image quality. We are developing patient-specific simulation methods that identify viable transcranial acoustic windows for intraoperative photoacoustic visualization of these underlying structures. Photoacoustic k-Wave simulations were performed based on a CT volume of an intact human cadaver head, which was later used to create experimental images of the internal carotid arteries. Acoustic receivers distributed across the eyelids measured pressure from intracranial photoacoustic sources. Differences in photoacoustic signal quality between the left and right eyelid receiver locations were investigated. Simulated sensors placed on the right eyelid received a 6.4 dB greater median acoustic energy than simulated sensors placed on the left eyelid, which was confirmed experimentally with a 14.5 dB greater DAS photoacoustic image amplitude with the ultrasound probe placed on the right eyelid rather than the left eyelid. Therefore, the ocular cavity is a viable acoustic window for photoacoustic-guided neurosurgeries with the potential to identify intrapatient, left-right asymmetries, supporting a new paradigm for performing patient-specific simulations prior to surgical guidance.

## 1. INTRODUCTION

Endoscopic transsphenoidal surgery is a minimally invasive technique in which instruments are inserted through the nasal cavity to drill through sphenoid bone and remove pituitary tumors.<sup>1</sup> During this procedure, critical structures such as the internal carotid arteries (ICAs), cranial nerves, and dura lie within millimeters of each other. Iatrogenic injury to these structures causes surgical complications such as ICA injury, cerebral spinal fluid leak, hemorrhage, stroke, cranial nerve paresis, and death.<sup>2</sup> Patients with aggressive, reoccurring tumors often require revision surgeries in which scarring, loss of natural anatomical markers, and disrupted ICA locations increase the risk of surgical complications in these revision surgeries to 11.4%.<sup>2</sup>

Intraoperative techniques, such as stereotactic guidance and endoscopy, are the gold standard for navigation within the skull base. However, these techniques suffer from two primary limitations. First, stereotactic guidance is susceptible to registration errors as the anatomy is disrupted and deviates from preoperative x-ray computed tomography (CT) or magnetic resonance (MR) images. Second, although endoscopy offers real-time snapshots of the surgical site, it does not provide visualization of subsurface structures in the surgical path. To address these two well-known limitations, our group is pioneering transcranial photoacoustic imaging as a promising neurosurgical intraoperative imaging technique for real-time visualization of the ICAs,<sup>3-9</sup> with supporting evidence of more general transcranial photoacoustic imaging additionally provided by other groups.<sup>10-12</sup> However, transcranial photoacoustic imaging is challenged by interactions with cranial bone, which degrade image quality.<sup>13-15</sup>

We previously developed and demonstrated a simulation methodology to identify naturally occurring acoustic windows in the adult human skull, namely the temporal, nasal, and ocular regions.<sup>7,8</sup> The ocular region was determined to be an optimal location and was subsequently used to successfully obtain images of the left carotid

artery (LCA) and right carotid artery (RCA) within a fresh human cadaver head. The work presented in this paper utilizes these experimental cadaver imaging results in combination with simulations studies to further investigate the eyelid as an acoustic receiver location. In particular, this work validates that simulations can potentially model patient-specific asymmetries in the skull base and predict photoacoustic image quality when using the eyelids as the receiver location.

## 2. METHODS

Three-dimensional photoacoustic simulations were performed using the k-Wave toolbox,<sup>16,17</sup> based on the CT volume of a human cadaver head. The CT volume was converted to heterogeneous density, speed of sound, and absorption prefactor volumes. Fig. 1 shows an axial slice of the heterogeneous speed of sound volume. The computational grid was defined with a symmetric voxel size of 0.3 mm x 0.3 mm x 0.3 mm. Acoustic wave propagation was simulated with a time increment of  $1.23 \times 10^{-8}$  seconds. No shear waves were included in these simulations.

Spherical 0.3 mm-diameter photoacoustic targets were positioned in the locations of the LCA and RCA. Each source was simulated independently. Acoustic sensors were distributed across the eyelids to receive intracranial photoacoustic signals, as shown in Fig. 1(a). The signal energy,  $E_s$ , received by each sensor was calculated as:

$$E_s = \sum_{n=0}^N |x_s(n)|^2, \quad E \in \mathbb{R}^{1 \times S} \quad (1)$$

where  $s$  is the sensor index,  $S$  is the total number of sensors,  $x_s(n)$  is the time domain pressure signal,  $N$  is the total simulation time in seconds, and  $E$  is the vector containing all  $E_s$ . The log-compressed signal energy,  $\hat{E}_s$ , was calculated as:

$$\hat{E}_s = 20 \log_{10} \left( \frac{E_s}{\max(E)} \right) \quad (2)$$

Simulation outputs were validated with experimental channel data obtained from the experimental procedure described in our previous publication.<sup>8</sup> In particular, an ultrasound transducer was placed on the eyelids of the cadaver head and an optical source was inserted through the nasal cavity, as illustrated in Fig. 1(b). Ultrasound

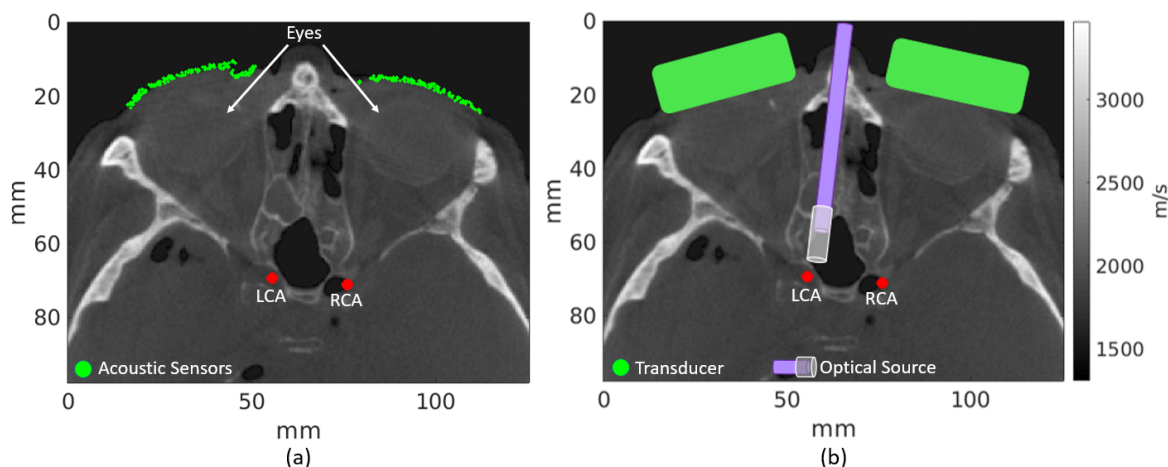


Figure 1: Annotated slices of the speed of sound distribution, derived from axial CT slices of the same human cadaver head. (a) The simulation consisted of acoustic sensors distributed across the eyelids and photoacoustic sources independently placed in the left carotid artery (LCA) or right carotid artery (RCA) position. (b) The corollary experimental setup consisted of transducers placed on the eyelids, an optical source inserted through the nasal cavity, and independently illuminated LCA and RCA photoacoustic sources.

and photoacoustic delay-and-sum (DAS) images were generated from the channel data and each image was normalized to its brightest pixel. Prior to normalizing the displayed photoacoustic DAS images, the amplitudes of the image pixels,  $P_i$ , within an ellipsoidal region of interest (ROI) inside the photoacoustic source were measured and converted to a log-compressed amplitude as follows:

$$\hat{P}_i = 20\log_{10}\left(\frac{P_i}{\max(P)}\right), \quad P \in \mathbb{R}^{1 \times I} \quad (3)$$

where  $i$  is the pixel index,  $I$  is the total number of pixels, and  $P$  is the vector containing all  $P_i$ .

### 3. RESULTS

Fig. 2 shows the photoacoustic signal energy received by each simulated acoustic sensor on the left and right eyelids, as calculated by Eq. 2. When the LCA was simulated, the left eye sensors received a higher median signal energy of -27.94 dB when compared to -34.99 dB for the right eye sensors, as demonstrated in Fig. 2(a). When the RCA was simulated, the right eye sensors received a higher median signal energy of -21.53 dB when compared to -36.33 dB for the left eye sensors, as demonstrated in Fig. 2(b). Based on these results, it would be most ideal to image the LCA and RCA with sensors located on the left and right eye, respectively. Fig. 2(c) compares the relative probability distributions of the log-compressed signal energies received by the sensors placed in the ideal imaging locations defined above. Although the left and right distributions share energy values in similar ranges (i.e., -41.81 dB to -6.11 dB and -44.05 dB to 0 dB, respectively), the right distribution is skewed toward higher energy measurements than the left distribution. In particular, the median of the right eye energy distribution is 6.41 dB greater than the median of the left eye energy distribution.

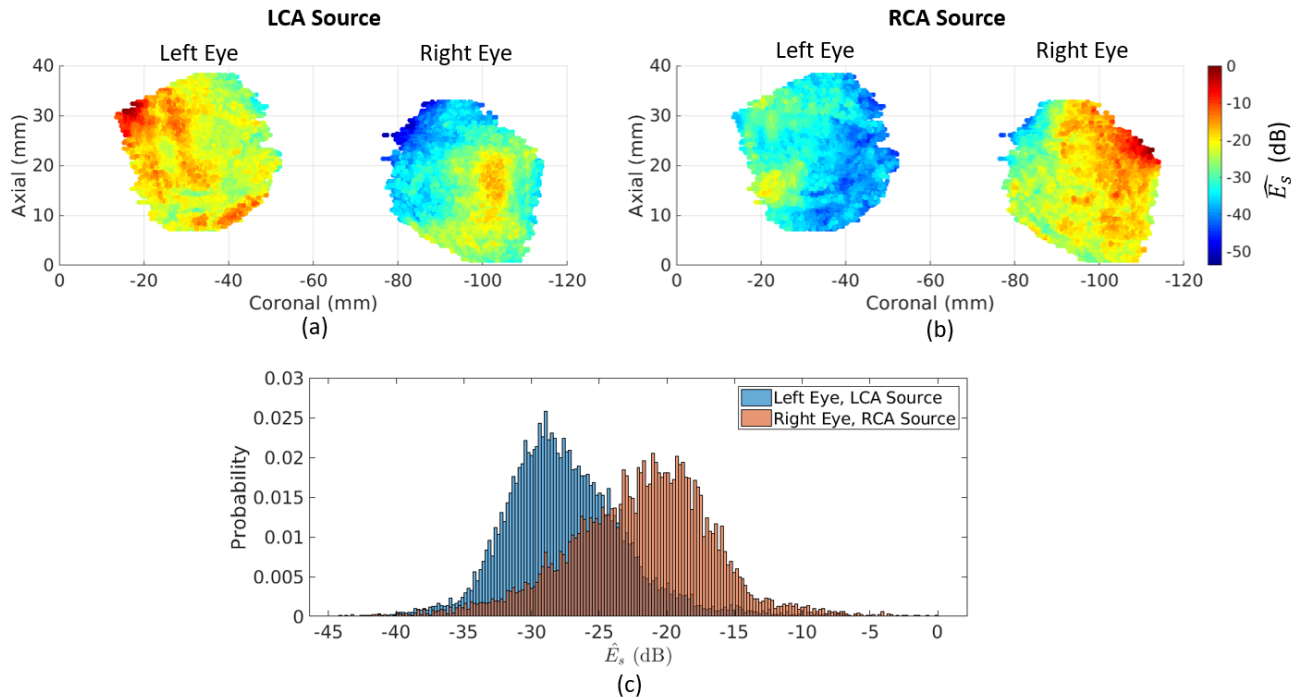


Figure 2: Visualization of k-Wave acoustic sensor data for sensors placed on the left and right eyelids of the cadaver head when the photoacoustic source is the (a) LCA and (b) RCA. (c) Histograms of the probability of a left or right eyelid sensor receiving a log-compressed total signal energy in the range 0 to -45 dB. Each histogram represents energies from sensors on a singular eyelid when illuminating the corresponding carotid artery independently, calculated using Eq. 2.

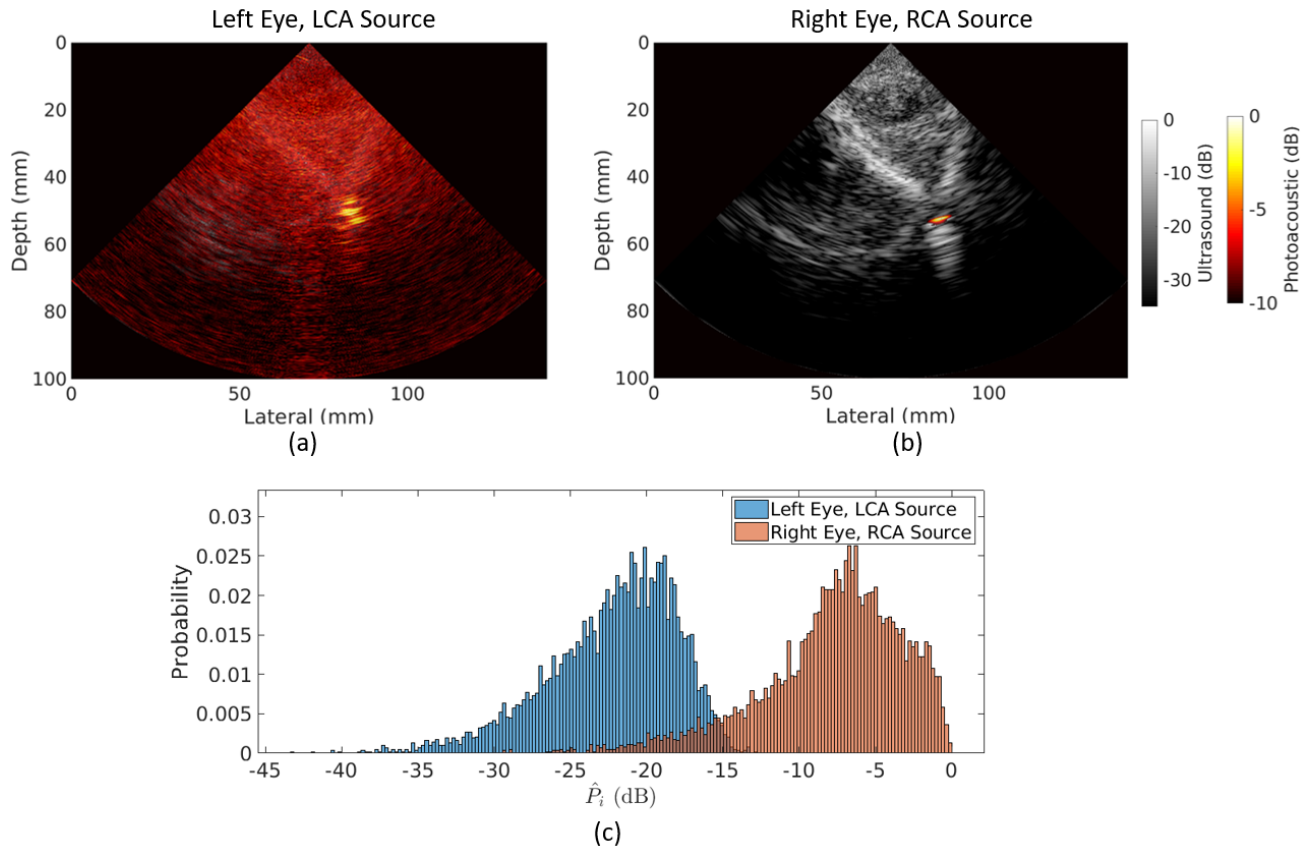


Figure 3: DAS photoacoustic images from the fresh cadaver, overlaid on co-registered ultrasound images when the transducer location and photoacoustic source are the (a) left eyelid and LCA and (b) right eyelid and RCA. The images were normalized to the brightest pixel within the image. (c) Histograms of the probability of an image pixel within a region of interest inside the photoacoustic source in the DAS images having an amplitude in the range 0 to -45 dB, calculated using Eq. 3.

Fig. 3 shows experimental photoacoustic results from the same human cadaver head that was simulated to obtain the results in Fig. 2. Photoacoustic images obtained from each eyelid probe position were overlaid on co-registered ultrasound images. When imaging from the left eye, background noise was present in the photoacoustic image, reducing the overall LCA visibility (Fig. 3(a)). When imaging from the right eye, less background noise was present, enabling better RCA visibility (Fig. 3(b)). Fig. 3(c) compares the relative probability distributions of the log-compressed photoacoustic image amplitudes from ROIs within the photoacoustic targets in Figs. 3(a) and 3(b), as calculated by Eq. 3. The right distribution is skewed toward higher amplitude measurements than left distribution. In particular, the distributions have amplitude values in the range -43.12 dB to -12.86 dB and -29.41 dB to 0 dB, for the left and right eye images, respectively. The median of the left and right image amplitude distributions are -21.55 dB and -7.05 dB, respectively.

#### 4. DISCUSSION

The work presented in this paper used experimental cadaver imaging to validate the predictions of simulation studies based on the same cadaver head. In particular, two predictions were made from the simulation results. First, it is optimal to place the acoustic receiver on the left and right eyelids when imaging the LCA and RCA, respectively (see Figs. 2(a) and 2(b)). Second, when using these optimal locations, there is a left-right asymmetry between the received energies for this particular patient (see Fig. 2(c)). The simulation study prediction of asymmetry was confirmed with experimental images, which demonstrated greater ICA visibility

and greater pixel amplitudes in the image obtained with the right eyelid probe location when compared to that of the left eyelid probe location (see Fig. 3). The left-right asymmetry is most likely due to anatomical differences in the acoustic pathways from the ICA sources to their respective ocular cavity opening. Therefore, the agreement between cadaver and simulation results demonstrates that simulations can potentially provide patient-specific predictions of photoacoustic image quality based on a patient's unique skull base anatomy.

In addition, results demonstrate the promise of photoacoustic simulations as a tool for patient-specific pre-operative surgical planning of optimal receiver locations when using photoacoustic imaging as an intraoperative navigation technique. Presurgical identification of receiver locations offers three primary benefits in photoacoustic image-guided surgery. First, this presurgical identification would eliminate wasting valuable operating room time to search for and find a suitable transducer location, thereby reducing the time the patient is under anesthesia, the total procedure duration, and the medical cost. The second benefit is removal of the potential barrier that the surgeon may be unable to identify a viable transducer location and therefore unable to use photoacoustic image-guidance during the procedure. The third benefit is identification of transducer locations which would minimize image quality degradation from the presence of bone and thereby produce photoacoustic images of the ICAs with the best image quality possible for the patient.

## 5. CONCLUSION

This paper is the first to use photoacoustic amplitude distributions from a human cadaver to validate that simulations sufficiently model patient-specific asymmetries in the skull base. Experimental results also demonstrate that simulations can predict photoacoustic image quality when using the eyelids as the receiver location. Photoacoustic energy measurements from simulations and amplitude measurements from experiments revealed that the right eyelid receiver location outperformed the left eyelid receiver location. These results highlight the promise of simulations as a patient-specific presurgical planning tool when using photoacoustic imaging as an intraoperative navigation technique.

## ACKNOWLEDGMENTS

This work was supported by NIH Grant No. R00-EB018994, NSF CAREER Award Grant No. ECCS 1751522, and the NSF Graduate Research Fellowship Program (Grant No. DGE1746891). The authors thank Peter Kazanzides for sharing the Mayfield clamp used to complete the cadaver experiment.

## REFERENCES

- [1] Cappabianca, P., Cavallo, L. M., and de Divitiis, E., "Endoscopic endonasal transsphenoidal surgery," *Neurosurgery* **55**, 933–941 (2004).
- [2] Agam, M. S., Wedemeyer, M. A., Wrobel, B., Weiss, M. H., Carmichael, J. D., and Zada, G., "Complications associated with microscopic and endoscopic transsphenoidal pituitary surgery: experience of 1153 consecutive cases treated at a single tertiary care pituitary center," *Journal of Neurosurgery* **130**(5), 1576–1583 (2018).
- [3] Bell, M. A. L., K.Ostrowski, A., Li, K., Kazanzides, P., and Boctor, E. M., "Localization of transcranial targets for photoacoustic-guided endonasal surgeries," *Photoacoustics* **3**(2), 78–87 (2015).
- [4] Bell, M. A. L., Ostrowski, A. K., Li, K., Kazanzides, P., and Boctor, E. M., "Quantifying bone thickness, light transmission, and contrast interrelationships in transcranial photoacoustic imaging," in [*Proceedings of SPIE, Photons Plus Ultrasound: Imaging and Sensing*], **9323** (2015).
- [5] Bell, M. A. L., Dagle, A. B., Kazanzides, P., and Boctor, E. M., "Experimental assessment of energy requirements and tool tip visibility for photoacoustic-guided endonasal surgery," in [*Proceedings of SPIE, Photons Plus Ultrasound: Imaging and Sensing*], **9708**, 97080D (2016).
- [6] Bell, M. A. L., Ostrowski, A. K., Kazanzides, P., and Boctor, E. M., "Feasibility of transcranial photoacoustic imaging for interventional guidance of endonasal surgeries," in [*Proceedings of SPIE, Photons Plus Ultrasound: Imaging and Sensing*], **8943**(894307) (2014).

- [7] Graham, M. T., Huang, J., Creighton, F., and Bell, M. A. L., “Simulations and human cadaver head studies to identify optimal acoustic receiver locations for minimally invasive photoacoustic-guided neurosurgery,” *Photoacoustics* , 100183 (2020).
- [8] Graham, M. T., Creighton, F. X., and Bell, M. A. L., “Investigation of acoustic windows for photoacoustic imaging of intracranial blood vessels,” in [2020 *IEEE International Ultrasonics Symposium (IUS)*], 1–4, IEEE (2020).
- [9] Lediju Bell, M. A., “Photoacoustic imaging for surgical guidance: Principles, applications, and outlook,” *Journal of Applied Physics* **128**(6), 060904 (2020).
- [10] Wang, X., Chamberland, D. L., and Xi, G., “Noninvasive reflection mode photoacoustic imaging through infant skull toward imaging of neonatal brains,” *Journal of Neuroscience Methods* **168**(2), 412–421 (2008).
- [11] Kirchner, T., Gröhl, J., Holzwarth, N., Herrera, M. A., Hernández-Aguilera, A., Santos, E., and Maier-Hein, L., “Photoacoustic monitoring of blood oxygenation during neurosurgical interventions,” in [*Proceedings of SPIE, Photons Plus Ultrasound: Imaging and Sensing*], **10878**, 14 – 18 (2019).
- [12] Kircher, M. F., De La Zerda, A., Jokerst, J. V., Zavaleta, C. L., Kempen, P. J., Mittra, E., Pitter, K., Huang, R., Campos, C., Habte, F., et al., “A brain tumor molecular imaging strategy using a new triple-modality mri-photoacoustic-raman nanoparticle,” *Nature Medicine* **18**(5), 829–834 (2012).
- [13] Kneipp, M., Turner, J., Estrada, H., Rebling, J., Shoham, S., and Razansky, D., “Effects of the murine skull in optoacoustic brain microscopy,” *Journal of Biophotonics* **9**(1-2), 117–123 (2016).
- [14] Pinton, G., Aubry, J.-F., Bossy, E., Muller, M., Pernot, M., and Tanter, M., “Attenuation, scattering, and absorption of ultrasound in the skull bone,” *Medical Physics* **39**(1), 299–307 (2012).
- [15] Estrada, H., Rebling, J., Turner, J., and Razansky, D., “Broadband acoustic properties of a murine skull,” *Physics in Medicine & Biology* **61**(5), 1932 (2016).
- [16] Treeby, B. E. and Cox, B. T., “k-Wave: MATLAB toolbox for the simulation and reconstruction of photoacoustic wave fields,” *Journal of Biomedical Optics* **15**(2), 021314 (2010).
- [17] Treeby, B. E., Cox, B. T., and Jaros, J., *A MATLAB toolbox for the time domain simulation of acoustic wave field, User manual, (2016) Manual Version 1.1, Toolbox Release 1.1.*